

# Extrinsic Pseudocapacitive Ternary NiMoO<sub>4</sub>-rGO@V<sub>2</sub>O<sub>5</sub> Nanocomposite for Hybrid Supercapacitor

Digambar S. Sawant, Shubham Patil, Mahesh Chougale, Abhishek Kulkarni, Niroshan Manoharan, Akash Fulari, Sarfraz Mujawar, Shrinivas B. Kulkarni,\* and Gaurav M. Lohar\*

Battery-type electrode materials with exceptionally high specific energy have been recognized as prospective materials for hybrid supercapacitor (HSC). In this study, a ternary NiMoO<sub>4</sub>-rGO@V<sub>2</sub>O<sub>5</sub> composite is synthesized for high performance HSC applications. The strategic integration of nickel molybdate (NiMoO<sub>4</sub>), reduced graphene oxide (rGO), and vanadium pentoxide (V<sub>2</sub>O<sub>5</sub>) combines the fast-redox activity of NiMoO<sub>4</sub>, the high electrical conductivity and surface area of rGO, and the excellent pseudocapacitive behavior of V<sub>2</sub>O<sub>5</sub>. The NiMoO<sub>4</sub>-rGO@V<sub>2</sub>O<sub>5</sub> composite obtains pore structure ranging from 20–30 nm with a higher specific surface area of 176.2 m<sup>2</sup> g<sup>-1</sup> and superior conductivity, demonstrating enhanced capabilities regarding the transfer of charge and

diffusion of ions. Electrochemical measurements demonstrate that the NiMoO<sub>4</sub>-rGO@V<sub>2</sub>O<sub>5</sub> composite exhibits a high specific capacity of 361.5 mAh g<sup>-1</sup> at 1 A g<sup>-1</sup>, excellent rate capability, and remarkable cyclic stability of 75% after 10,000 cycles. Furthermore, an HSC device assembled using the optimized composite as the positive electrode and activated carbon as the negative electrode and it delivered a capacitance of 207.5 F g<sup>-1</sup> at 2 mA cm<sup>-2</sup> with a specific energy of 73.77 Wh kg<sup>-1</sup> at a specific power of 640 W kg<sup>-1</sup>. These outcomes underscore the potential of NiMoO<sub>4</sub>-rGO@V<sub>2</sub>O<sub>5</sub> composites as cutting-edge electrode materials for next-generation energy storage devices.

## 1. Introduction

In recent years, as technology continues to advance rapidly and with an increasing use of portable and renewable energy-driven devices, the need for safe, efficient energy storage systems has

increased exponentially. The rapid proliferation of smartphones, laptops, electric vehicles, along with the rest of the world's growing demand for portable electronics, has created a strong demand for energy storage solutions that are more compact, lighter weight, and higher performance. Furthermore, the ongoing global shift to more sustainable energy sources like solar and wind, which are inherently intermittent by nature, has only increased the need for dependable long-term energy storage solutions that can help provide a reliable, consistent energy supply. Further, with the emergence of smart grids and the Internet of Things (IoT), there is an increasing demand for these decentralized storage systems, which can react quickly to changes in energy demand and production.<sup>[1–4]</sup> These macro trends in technology and climate change and energy security have led to a tremendous amount of research into new materials and devices for advanced energy storage, like supercapacitors and batteries, to fulfill the rising specific power and energy needs of modern-day applications. Recently, in energy materials research, supercapacitors have become a popular focus, serving as intermediaries between capacitors and batteries for applications where rapid energy exchange, long lifecycle, and high dependability are essential.<sup>[5,6]</sup>

See similar supercapacitors, unlike batteries that are dependent on faradaic redox reactions, supercapacitors mainly use non-faradaic electrostatic charge storage in electric double-layer capacitors (EDLC) or surface confined redox reactions in pseudocapacitors, resulting in much faster charge transfer kinetics. This allows the resulting specific power to exceed 10 kW kg<sup>-1</sup>, rendering them advantageous for high-frequency charge-discharge

D. S. Sawant, S. B. Kulkarni  
Department of Physics  
The Institute of Science  
Dr. Homi Bhabha State University  
Madam Cama Road, Mumbai 400032, India  
E-mail: sbk\_physics@yahoo.com

D. S. Sawant, G. M. Lohar  
Department of Physics  
Lal Bahadur Shastri College of Arts, Science and Commerce  
Satara 415002, India  
E-mail: gauravlohar24@gmail.com

S. Patil, M. Chougale, A. Kulkarni, N. Manoharan  
Centre for Materials Science  
School of Chemistry and Physics  
Queensland University of Technology (QUT)  
2 George Street, Brisbane QLD 4000, Australia

A. Fulari  
Symbiosis Centre for Nanoscience and Nanotechnology  
Symbiosis International (Deemed University)  
Pune 412115, India

S. Mujawar  
Department of Physics  
Yashavantrao Chavan Institute of Science Satara  
(Autonomous), Karmaveer Bhaurao Patil University  
Satara 415001, India

 Supporting information for this article is available on the WWW under <https://doi.org/10.1002/batt.202500423>

cycles. Furthermore, the absence of phase transformation or ion diffusion across bulk electrode materials ensures minimal structural degradation, allowing supercapacitors to retain performance over  $>10^5\text{--}10^6$  cycles with almost negligible capacity fading, attributes that are critical for applications such as pulsed power systems, active load leveling, and autonomous sensors in IoT environments.<sup>[7–9]</sup> An extrinsic pseudocapacitor refers to a type of pseudocapacitive behavior displayed by nanostructured battery-type materials used in supercapacitor applications. These materials show battery-like faradaic redox reactions involving bulk intercalation or phase changes, but can exhibit pseudocapacitive electrochemical features such as distinct redox peaks in cyclic voltammetry (CV) and voltage plateaus in galvanostatic charge-discharge (GCD) curves, resembling battery behavior. Essentially, extrinsic pseudocapacitors are hybrid devices combining battery-type electrodes with capacitive properties, often utilized in hybrid supercapacitor (HSC) to achieve higher specific energy than conventional capacitors. This contrasts with intrinsic pseudocapacitors, where charge storage is dominated by fast, reversible surface, or near-surface redox reactions without bulk diffusion or phase changes.<sup>[10,11]</sup> Nickel based oxides,<sup>[12]</sup> sulfides,<sup>[13]</sup> metal organic frameworks,<sup>[14]</sup> and layer double hydroxide<sup>[15]</sup> are some typical examples of extrinsic pseudocapacitors, which show these battery-type faradaic processes at the nanoscale level but also behave like pseudocapacitors in electrochemical tests.

Furthermore, the versatility of supercapacitor electrode materials ranging from carbonaceous nanostructures and transition metal oxides ( $\text{NiMoO}_4$  &  $\text{V}_2\text{O}_5$ ) to their hybrid composites provides tunable electrochemical characteristics that can be customized to specific application needs.<sup>[16–18]</sup> Innovative structures such as hierarchical porous networks, core shell morphologies, and interrally engineered composites drastically improve ion diffusion kinetics and electroactive surface area, mitigating the high specific energy issue typically associated with supercapacitors.  $\text{NiMoO}_4$  is a mixed transition metal oxide, provides a wealth of redox activity, various oxidation states ( $\text{Ni}^{2+}/\text{Ni}^{3+}$ ), and high theoretical specific capacity, appearing as an optimal pseudocapacitive material. Its practical performance is usually severely challenged by low electrical conductivity and poor structural stability during long-term cycling.<sup>[19–21]</sup> The introduction of reduced graphene oxide (rGO) tackles these issues flawlessly through the use of a conductive, flexible, and mechanically strong support matrix. The rGO contributes to enhancing the electron transport and buffers the volume change occurring in charge-discharge cycle, which leads to high rate capability and long-term cycling stability.<sup>[22–24]</sup> Excepting lately little have been researched of  $\text{NiMoO}_4$ -rGO composites coupled with other materials for supercapacitors. Additionally, the further incorporation of vanadium pentoxide ( $\text{V}_2\text{O}_5$ ) into the  $\text{NiMoO}_4$ -rGO framework greatly improves the electrochemical performance. The  $\text{V}_2\text{O}_5$  obtained a high theoretical capacitance and a layered crystal structure that promotes rapid ion intercalation and diffusion. The  $\text{V}_2\text{O}_5$  adds extra redox active sites through  $\text{V}^{5+}/\text{V}^{4+}$  transitions, thus enhancing total charge storage capacity.<sup>[25,26]</sup> The synergistic interaction

between  $\text{NiMoO}_4$ -rGO and  $\text{V}_2\text{O}_5$  results in a hierarchical composite architecture with plentiful electroactive interfaces, enhanced electrolyte accessibility, and shortened ion/electron transport pathways. This multicomponent hybrid system allows a desirable trade-off between specific energy and specific power, overcoming the drawbacks of single-phase materials.  $\text{NiMoO}_4$ -rGO@ $\text{V}_2\text{O}_5$  composites stand for a practical progress toward high performance, durable and scalable electrode materials for next-generation HSC devices.

The sol-gel method appears to be one of the most popular one-step processes for the synthesis of nanomaterials because of its versatility, simplicity, and capability to prepare materials with high purity, homogeneity, and controlled nanostructure. These mild processing conditions are particularly beneficial when attempting to synthesize metal oxides, complex composites, or doped materials that do not undergo undesired phase transformations or thermal degradation. Among these methods, one of the main advantages of the sol-gel method is its appropriateness for producing nanomaterials with controlled porosity and wide surface area, which are critical features for electrochemical energy storage applications such as supercapacitors.<sup>[27,28]</sup> Because of the molecular level mixing of precursors in the sol phase, it not only makes the distribution of active elements uniform but ensures the formation of a multicomponent system that is homogeneous on a molecular scale, such as  $\text{NiMoO}_4$ -rGO@ $\text{V}_2\text{O}_5$ . From the literature (Table 1), there is a wide scope to develop the  $\text{NiMoO}_4$ -rGO composite with  $\text{V}_2\text{O}_5$  and its study for supercapacitor performance. So, we have successfully synthesis of a ternary  $\text{NiMoO}_4$ -rGO@ $\text{V}_2\text{O}_5$  composite via a sol-gel route. The synergistic combination of the conductive rGO framework, the high-capacity  $\text{NiMoO}_4$ , and the pseudocapacitive  $\text{V}_2\text{O}_5$  results in a composite with superior electrochemical properties. This study discusses the influence of  $\text{V}_2\text{O}_5$  on  $\text{NiMoO}_4$ -rGO composite with their structural, morphological, and electrochemical performance. The NMO-rGO@ $\text{V}_2\text{O}_5$  composites delivered higher specific capacity, long-term cyclic performance. Also, the HSC displays enormous characteristics, including high specific energy and power, and higher cyclic stability performance.

## 2. Experimental Section

### 2.1. Materials

Analytical grade nickel nitrate hexahydrate ( $\text{Ni}(\text{NO}_3)_2 \cdot 6\text{H}_2\text{O}$ ), sodium molybdate dihydrate ( $\text{Na}_2\text{MoO}_4 \cdot 2\text{H}_2\text{O}$ ), potassium hydroxide (KOH), graphite powder,  $\text{V}_2\text{O}_5$ , polyvinylidene fluoride (PVDF), carbon black, and N-methyl-2-pyrrolidone (NMP) were purchased from Thomas Baker Pvt. Ltd. Company and used in this study without additional purification. For electrode material preparation, a highly conducting nickel foam substrate was used as a current collector was procured from Sigma Aldrich, Company. Double distilled water (DDW) was used as a solvent to prepare solutions.

**Table 1.** Comparative electrochemical performance of NiMoO<sub>4</sub> based materials.

Electrode material	Morphology	Specific capacitance [ $\text{F g}^{-1}$ ]	Calculated Specific capacity [ $\text{mAh g}^{-1}$ ]	Cyclic stability	Electrolyte	Reference
NiMoO <sub>4</sub>	Nanoflowers	1092	97.2	91% after 2000 cycles	6M KOH	[21]
NiMoO <sub>4</sub>	Microspheres	1520	168.9	80% over 7000 cycles	2 M KOH	[18]
NiMoO <sub>4</sub>	Nanosheets	864	13.9	71% after 1000 cycles	2M KOH	[49]
NiMoO <sub>4</sub> @rGO	NiMoO <sub>4</sub> nanoflowers on rGO nanosheets	1400	194.4	91% after 2000 cycles	6M KOH	[21]
NiMoO <sub>4</sub> @rGO	NiMoO <sub>4</sub> nanosheets on rGO nanosheets	1888	251.7	95% after 2300 cycles	2M KOH	[24]
NiMoO <sub>4</sub> @rGO	NiMoO <sub>4</sub> nanowires on rGO nanosheets	1194	165.8	89.2% over 500 cycles	3M KOH	[23]
NiMoO <sub>4</sub> /rGO/PANI	Hydrangea like structure	2300	319.44	72.2% after 5000 cycles	3M KOH	[50]
NiMoO <sub>4</sub> @rGO	Microspheres on rGO nanosheets	2033	225.9	71% over 10,000 cycles	2M KOH	This work
70:30 NMO-rGO@V <sub>2</sub> O <sub>5</sub>	Nanocomposite on rGO nanosheets	3253	361.5	75% over 10,000 cycles	2M KOH	

## 2.2. Synthesis of NiMoO<sub>4</sub>-rGO by Hydrothermal Method

The NiMoO<sub>4</sub>-rGO composites were synthesized by one step hydrothermal treatment. Graphene oxide (GO) was synthesized from natural graphite flakes by a modified Hummer's method.<sup>[29]</sup> In a synthesis of 10 mM Ni(NO<sub>3</sub>)<sub>2</sub>·6H<sub>2</sub>O and 10 mM Na<sub>2</sub>MoO<sub>4</sub>·2H<sub>2</sub>O was dissolved in 30 ml DDW in different glass beakers, stirred for 30 min, then mixed and stirred for 15 min. Simultaneously, 1 mg ml<sup>-1</sup> GO powder were dissolved in 30 ml DDW and it ultrasonicated by a probe sonicator to disperse GO sheets for 30 min ( $T_{\text{on}} = 5 \text{ s}$ ,  $T_{\text{off}} = 2 \text{ s}$ , 100 W). The two prepared solutions were mixed and once again ultrasonicated for 30 min. Afterward, the hydrothermal reaction was carried out at 160 °C for 6 h. The prepared powder was dried at 60 °C in the oven for 24 h and annealed at 400 °C for 2 h in an air atmosphere.

## 2.3. Synthesis of NiMoO<sub>4</sub>-rGO@V<sub>2</sub>O<sub>5</sub> Composite by Sol-gel Method

The prepared NiMoO<sub>4</sub>-rGO was first dispersed in some amount of ethanol and ultrasonicated for 30 min. Subsequently, V<sub>2</sub>O<sub>5</sub> powder was dispersed in some amount of ethanol and

ultrasonicated to obtain a uniform suspension. The proportion of NiMoO<sub>4</sub>-rGO is varying the weight ratio with adding the V<sub>2</sub>O<sub>5</sub> powder as (80:20, 70:30, and 60:40). Then, these two solutions are mixed together and ultrasonicated again for 30 min. After that the mixed solution was heated at a certain temperature to remove the solvent from it. Then the resulting powder was dried at 60 °C overnight in an air atmosphere. The schematic representation of the synthesis of NMO-rGO@ V<sub>2</sub>O<sub>5</sub> by sol-gel method is shown in Figure 1.

## 2.4. Material Characterization

The structural properties of the materials were studied using X-ray diffraction (XRD), Raman spectroscopy, and X-ray photoelectron spectroscopy (XPS) and morphological properties were examined by using scanning electron microscopy (SEM), transmission electron microscopy (TEM). To identify surface area and pore size using Brunauer–Emmett–Teller (BET) techniques. The electrochemical workstation Biologic Sp-300 is used to investigate electrochemical performance with CV, GCD, and electrochemical impedance spectroscopy (EIS) in a three-electrode configuration.

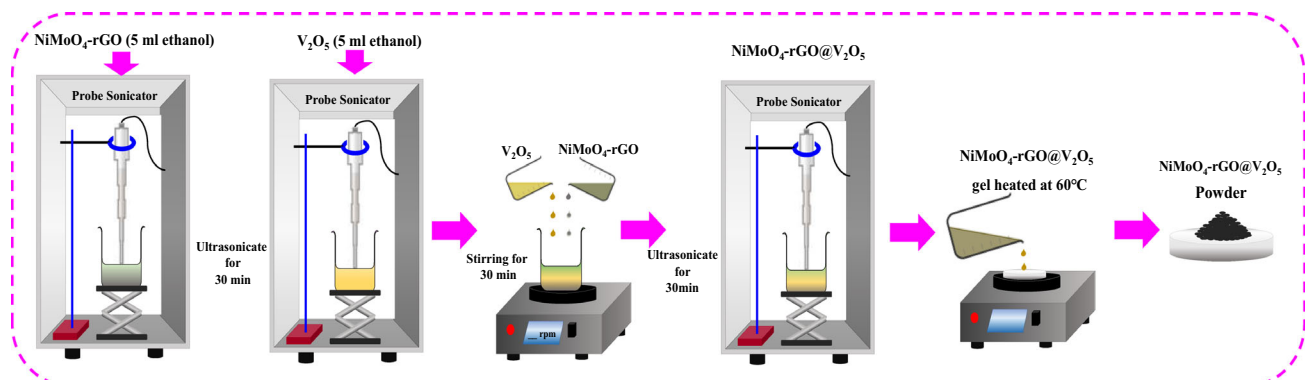


**Figure 1.** Schematic presentation of synthesis of NMO-rGO@V<sub>2</sub>O<sub>5</sub> by simple Sol-Gel method.

### 2.4.1. Preparation of Electrode

In an ultrasonication bath, a piece of nickel foam ( $3 \times 1$  cm) was cleaned with HCl, ethanol, and DDW each for 10 min respectively, and dried overnight at  $60^\circ\text{C}$  in the oven. The actual electrode was prepared by mixing prepared  $\text{NiMoO}_4$ -rGO@ $\text{V}_2\text{O}_5$  powders (active material), PVDF as a binder, and carbon black in a ratio of 80:10:10. Then, a sufficient amount of NMP as solvent was mixed to obtain a uniform slurry. Afterward, the prepared slurry was coated on nickel foam ( $1 \times 1$  cm) and subjected to  $80^\circ\text{C}$  in a hot air oven for 12 h. The mass of  $\text{NiMoO}_4$ -rGO@ $\text{V}_2\text{O}_5$  loaded on NF was about  $1.4 \text{ mg cm}^{-2}$  to assure the repeatability of the performance. These prepared electrodes were used for an electrochemical supercapacitor study.

The specific capacity in  $\text{mAh g}^{-1}$  of the  $\text{NiMoO}_4$ -rGO@ $\text{V}_2\text{O}_5$  nickel foam electrode was calculated by using the following Equation (1) from the GCD study<sup>[30]</sup>

$$\text{Specific capacity } (\text{mAh g}^{-1}) = \frac{I \times \Delta t}{3.6 \times m} \quad (1)$$

where  $I$  is applied current at charge-discharge process (mA),  $\Delta t$  is discharging time (s), and  $m$  is the actual mass of material are present on the working electrode (mg). All electrochemistry has been done in 2 M KOH electrolyte.

### 2.4.2. Fabrication of Hybrid Supercapacitor

HSC device is developed by using  $\text{NiMoO}_4$ -rGO@ $\text{V}_2\text{O}_5$  optimized electrode sample as the positive electrode and activated carbon (AC) as the negative electrode material in an aqueous 2 M KOH electrolyte. The negative electrode was prepared by using AC as active material, carbon black and PVDF as binder in a mass ratio of 80:10:10, with NMP was used as solvent and all were crushed in

an agate mortar. The prepared slurry of the material was coated on precleaned  $1 \times 1 \text{ cm}^2$  nickel foam. The mass of the negative electrode is  $1.1 \text{ mg cm}^{-2}$ . The charge balance in HSC design was ensured by calculating the electroactive mass ratio of  $\text{NiMoO}_4$ -rGO to AC from Equation (2), which was found to be 1.4:1.1. So, the total mass of the HSC device is 2.5 mg. The specific energy and specific power of the HSC were calculated by using following Equation (3) and (4)<sup>[31,32]</sup>

$$\frac{m_+}{m_-} = \frac{S_c \times \Delta V_-^2}{S_c \times \Delta V_+^2} \quad (2)$$

$$E_s = \frac{1}{7.2} S_c \Delta V^2 \quad (3)$$

$$P_s = \frac{E_s}{\Delta t} \quad (4)$$

where positive and negative signs indicate the anode and cathode, respectively.  $\Delta V$  is the voltage window of GCD study,  $S_c$  is the specific capacitance in  $\text{F g}^{-1}$  from GCD study,  $E_s$  is the specific energy in  $\text{Wh kg}^{-1}$ , and  $P_s$  is the specific power in  $\text{W kg}^{-1}$ .

## 3. Results and Discussion

### 3.1. X-Ray Diffraction Study

The XRD pattern shows the crystalline nature and material phase formation of all the synthesized samples of coded NMO-rG and 80:20, 70:30, 60:40 NMO-rGO@ $\text{V}_2\text{O}_5$  composites are displayed in Figure 2a. The presence of diffraction peaks at (110), (-112), (220), (221), and (440) attributed to  $\text{NiMoO}_4$  (JCPDS No. 01-086–0361) indicates that monoclinic  $\text{NiMoO}_4$  with

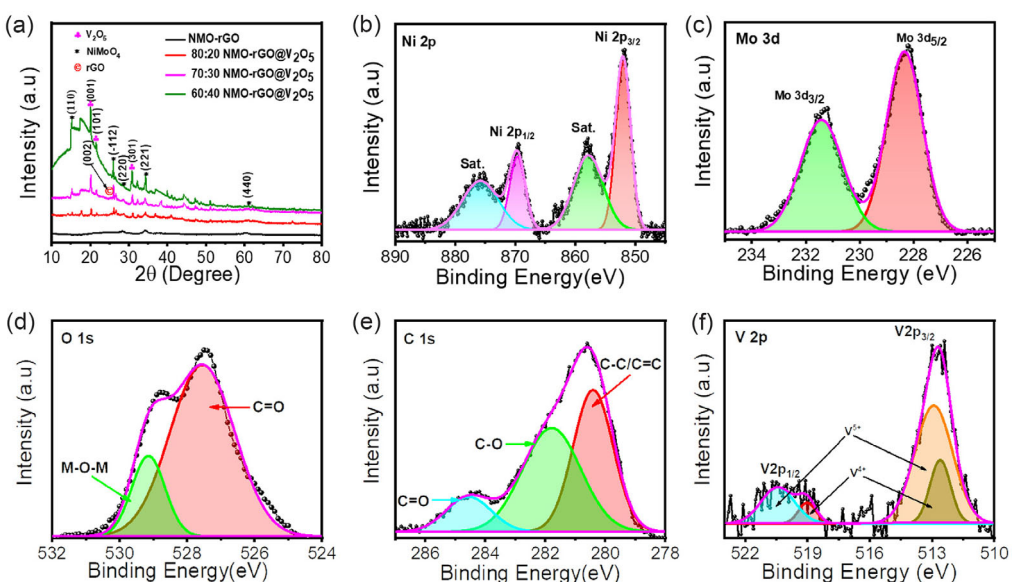


**Figure 2.** a) X-ray diffraction pattern of  $\text{NiMoO}_4$ -rGO@ $\text{V}_2\text{O}_5$  composite, X-ray photoelectron core level spectra for b) Ni 2p, c) Mo 3d, d) O 1s, e) C 1s, and f) V 2p, respectively, of optimized  $\text{NiMoO}_4$ -rGO@ $\text{V}_2\text{O}_5$  sample.

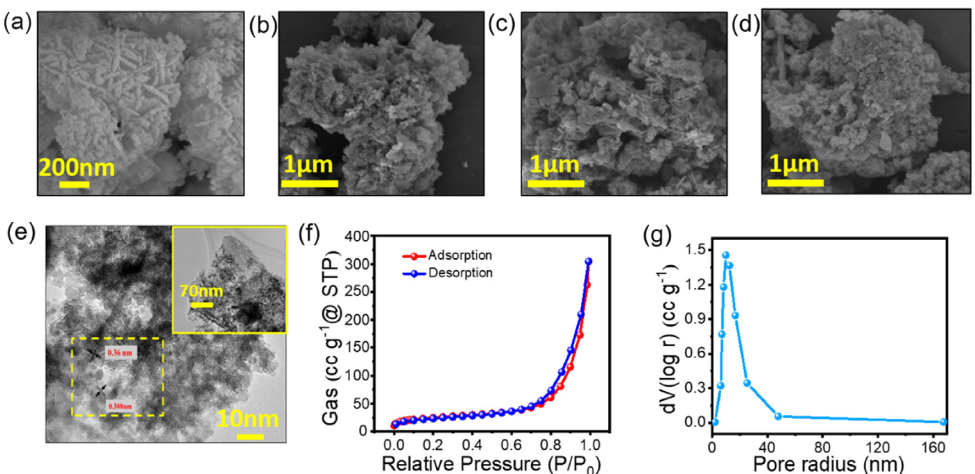


**Figure 3.** a–d) Scanning electron microscopy images of NiMoO<sub>4</sub>-rGO, 80:20 NMO-rGO@V<sub>2</sub>O<sub>5</sub>, 70:30 NMO-rGO@V<sub>2</sub>O<sub>5</sub>, and 60:40 NMO-rGO@V<sub>2</sub>O<sub>5</sub> respectively. e) Transmission electron microscopy images of optimized NMO-rGO@V<sub>2</sub>O<sub>5</sub> sample at various magnifications (inset). f,g) Nitrogen adsorption/desorption isotherms and BJH pore size distribution of optimized NMO-rGO@V<sub>2</sub>O<sub>5</sub> sample.

C2/m space group is successfully formed with clear and sharp reflections at  $2\theta$  values nearly consistent with the standard pattern.<sup>[33]</sup> With the introduction of rGO, the wide hump around  $26^\circ$  for (002) planes, which reflects some amorphous carbon, represents the successful combination of rGO and NiMoO<sub>4</sub>.<sup>[34]</sup> Further addition of V<sub>2</sub>O<sub>5</sub> into the composite is reflected by other peaks at (110), (001), (101), and (301) related to the orthorhombic phase of V<sub>2</sub>O<sub>5</sub> (JCPDS No. 41–1426), confirming the successful decoration of NMO-rGO surface with V<sub>2</sub>O<sub>5</sub> nanostructures.<sup>[35]</sup>

### 3.2. X-Ray Photoelectron Spectroscopy

The XPS analysis was performed to investigate the surface chemical composition and oxidation states of elements present in the NMO-rGO@V<sub>2</sub>O<sub>5</sub> composite material, as shown in Figure 2b–f. Wide survey elemental analysis clearly recapitulates the incorporation of Ni, Mo, O, C, and V elements, verifying the effective loading of V<sub>2</sub>O<sub>5</sub> and rGO with NiMoO<sub>4</sub> structure (Figure S1, Supporting Information). The high-resolution Ni 2p spectrum reveals two characteristic peaks at 855.6 and 873.1 eV can be assigned to Ni 2p<sub>3/2</sub> and Ni 2p<sub>1/2</sub>, respectively, along with the characteristic satellite peaks, confirming the presence of Ni<sup>2+</sup> species (Figure 2b). Mo 3d spectrum shows peaks at 232.3 eV (3d<sub>5/2</sub>) and 235.4 eV (3d<sub>3/2</sub>), corresponding to Mo<sup>6+</sup> oxidation states (Figure 2c). The energy difference between two energy levels for the Ni element is 17.5 eV and for the Mo element 3.1 eV.<sup>[36,37]</sup> O 1 s spectrum shows (Figure 2d) two dominant peaks at 529.5 and 531.2 eV, which can be attributed to lattice oxygen (M—O—M) and surface adsorbed oxygen (C=O), respectively. The deconvoluted C 1 s spectrum shows (Figure 2e) peaks at 284.6, 286.4, and 288.5 eV which are attributed to C—C/C=C, C—O, and C=O bonds, confirming the presence of rGO.<sup>[38]</sup> In the case of the V 2p spectrum, two peaks are clearly distinguishable at 516.4 and 523.8 eV, corresponding to V 2p<sub>3/2</sub> and V 2p<sub>1/2</sub>, respectively, with components due to V<sup>4+</sup> and V<sup>5+</sup> oxidation states confirming the presence of mixed-valence vanadium species in V<sub>2</sub>O<sub>5</sub>.

(Figure 2f).<sup>[39]</sup> These results confirm the successful formation of the NMO-rGO@V<sub>2</sub>O<sub>5</sub> composite with the intended elemental composition and chemical states, key for improving electrochemical performance.

### 3.3. Scanning Electron Microscopy

The surface morphology of the synthesized samples was explored using SEM, as shown in Figure 3a–d. The microsphere formed from the agglomeration of rod-shaped units of the pristine NiMoO<sub>4</sub> is uniformly distributed on the rGO sheets, is shown in Figure 3a, reflecting the favorable interaction between the NiMoO<sub>4</sub> and conductive rGO matrix. Upon adding V<sub>2</sub>O<sub>5</sub> at increasing ratios, a morphological transition from. For the 80:20 NMO-rGO@V<sub>2</sub>O<sub>5</sub> sample (Figure 3b), the surface seems to be more compact with less sphere through the nanorods clarity. The 70:30 NMO-rGO@V<sub>2</sub>O<sub>5</sub> composite, as shown in Figure 3c shows a uniform distribution of microspheres formed with interconnected nanorods, creating a loose and open framework. Increased amounts of V<sub>2</sub>O<sub>5</sub> cause agglomeration in the 60:40 NMO-rGO@V<sub>2</sub>O<sub>5</sub> (Figure 3d), producing a comparatively bulkier and less porous structure. The SEM images validate the desired porous and hierarchical morphology of 70:30 NMO-rGO@V<sub>2</sub>O<sub>5</sub> composite material, ensuring an ideal trade-off between conductivity and ion penetration.

### 3.4. Transmission Electron Microscopy

TEM analysis was conducted to investigate the internal structure and nanoscale arrangement of the optimized 70:30 NMO-rGO@V<sub>2</sub>O<sub>5</sub> composite (Figure 3e). The corresponding low-magnification TEM image (inset) shows a crumpled, highly porous and loosely packed network along with ultrafine V<sub>2</sub>O<sub>5</sub> nanoparticles homogeneously dispersed on the surface of NMO-rGO sheets. Intense high-magnification TEM images show a homogeneously dispersed scattering of nanocrystalline domains distributed inside the graphene matrix. The resulting experimental

interplanar lattice spacings of 0.36 nm could be attributed to the (110) plane of the orthorhombic  $V_2O_5$  and the 0.308 nm attributed to (002) plane of the monoclinic NMO-rGO.<sup>[33,35]</sup> This reflects the presence of both phases and their excellent interface coupling in the composite. This highly-embedded architecture serves to increase the electronic conductivity and promote charge transfer pathways within the composite. The intimate interaction between these nanocrystalline domains and the rGO matrix is necessary to offer greater electrical conductivity and facilitate rapid electron transfer through the heterostructure. The fine particle size and the uniform dispersion are likely to play a key role in enhancing electroactive surface area and electrochemical performance.<sup>[40]</sup>

### 3.5. Brunauer–Emmett–Teller Analysis

The surface area and pore structure of the optimized sample were studied using BET and Barrett–Joyner–Halenda (BJH) methods (Figures 3f,g). The nitrogen adsorption–desorption isotherms exhibit a type-IV curve with H3 hysteresis loop, confirming mesoporous property.<sup>[41]</sup> The high specific surface area of 176.2  $m^2 g^{-1}$  of optimized 70:30 NMO-rGO@ $V_2O_5$  samples is beneficial with abundant active sites for electrochemical reaction. The BJH pore size distribution curve shows a relatively sharp distribution mainly between 20–30 nm, which is ideal for electrolyte ion diffusion. These mesopores allow for high speed ion transport and diffusion resistance is decreased, leading to improved rate capability and cycling stability in supercapacitor application.<sup>[42]</sup> A BET analysis shows a large surface area and perfect mesoporous structure that promotes rapid ion diffusion and enhances the quantity of electrochemically active sites.

These structural and morphological characteristics work together to provide a synergistic effect that leads to an improved specific capacity, rate capability, and cyclic durability for the 70:30 composition compared to the other mixed ratios with either insufficient or excessive  $V_2O_5$  content.

### 3.6. Electrochemical Supercapacitor Study

The overall electrochemical study using CV and GCD techniques of the NMO-rGO and NMO-rGO@ $V_2O_5$  composites are displayed in Figure 4a–d. The comparative CV profiles of NiMoO<sub>4</sub>-rGO and NMO-rGO@ $V_2O_5$  composites with varying weight ratios (80:20, 70:30, and 60:40) were recorded at a scan rate of 5  $mV s^{-1}$  to investigate the redox behavior and capacitive performance (Figure 4a). All samples exhibited pronounced redox peaks, indicating a pseudocapacitive charge storage mechanism governed by faradaic redox reactions involving  $Ni^{2+}/Ni^{3+}$  transitions, along with redox activity from  $V_2O_5$ .<sup>[43]</sup> Among them, the 70:30 NMO-rGO@ $V_2O_5$  electrode sample delivered the largest integrated area under the CV curve, which is directly proportional to the highest specific capacity. The enhanced area suggests an optimal balance between active material utilization and electron/ion transport, facilitated by sufficient rGO content for conductivity and accessible electroactive sites due to the homogeneous distribution of

$V_2O_5$ . The sharper and more symmetric redox peaks of the 70:30 electrode further indicate superior electrochemical reversibility and lower polarization losses compared to other compositions. The comparative GCD curves of all electrodes were recorded at a constant current density of 1  $A g^{-1}$ , as shown in Figure 4b. The 70:30 NMO-rGO@ $V_2O_5$  electrode sample exhibited the longest discharge time, signifying the highest specific capacity among the tested electrodes. This enhanced charge storage performance can be attributed to the synergistic interaction between NiMoO<sub>4</sub> nanostructures and well-dispersed  $V_2O_5$  integrated into the rGO matrix. The GCD profiles of all electrodes show nonlinear shapes with distinct plateaus, confirming the pseudocapacitive nature of charge storage. The reduced IR drop observed in the 70:30 electrode also reflects its improved electrical conductivity and minimal internal resistance, which can be ascribed to the optimized ratio of conductive graphene and active material. The combination of low resistance, enhanced redox activity, and better ion diffusion kinetics results in the superior performance of the 70:30 NMO-rGO@ $V_2O_5$  composition.<sup>[44]</sup> The superior electrochemical behavior of the 70:30 NMO-rGO@ $V_2O_5$  electrode is a consequence of the optimized hybrid structure where the relative proportion of  $V_2O_5$  enhances redox activity without causing particle agglomeration or hindering ion transport. Compared to 80:20 NMO-rGO@ $V_2O_5$ , the higher  $V_2O_5$  content in 70:30 NMO-rGO@ $V_2O_5$  sample and increases the number of active redox sites, while maintaining sufficient rGO to preserve high electronic conductivity. On the other hand, in the 60:40 NMO-rGO@ $V_2O_5$  material composition, excessive  $V_2O_5$  may lead to poor contact between active components and hinder electrolyte accessibility due to dense packing or partial restacking, which reduces performance. Thus, the 70:30 ratio of NMO-rGO@ $V_2O_5$  presents a critical balance, enabling efficient charge transport, abundant electroactive sites, and robust electron pathways for enhanced capacitive behavior.

The CV curves at different scan rates (5–100  $mV s^{-1}$ ) of the optimized 70:30 NMO-rGO@ $V_2O_5$  sample are shown in Figure 4c and it retain their pseudocapacitive features with distinct redox peaks, suggesting good reversibility and rate capability. Figure S2a–c, Supporting Information represents the CV curves of NMO-rGO, 80:20 NMO-rGO@ $V_2O_5$  and 60:40 NMO-rGO@ $V_2O_5$  at different scan rates (5–100  $mV s^{-1}$ ). The GCD curves at various current densities of 70:30 NMO-rGO@ $V_2O_5$  electrode sample (Figure 4d) show quasisymmetric charge–discharge profiles, further confirming the pseudocapacitive behavior and good electrochemical reversibility. Figure S3a–c represents the GCD curves of NMO-rGO, 80:20 NMO-rGO@ $V_2O_5$ , and 60:40 NMO-rGO@ $V_2O_5$  at different current densities (1–5  $A g^{-1}$ ). The superior electrochemical performance of the 70:30 NMO-rGO@ $V_2O_5$  composite is further supported by morphological and surface area characterization. From the SEM images, it can be inferred that this sample has a consistent and well fabricated interconnected nanostructure with well dispersed  $V_2O_5$  throughout the NMO-rGO matrix, which prevents the agglomeration observed in the 60:40 ratio. This type of architecture allows for improved electrolyte penetration, enabling more efficient use of electroactive sites. Supporting this, TEM analysis reiterates this observation more

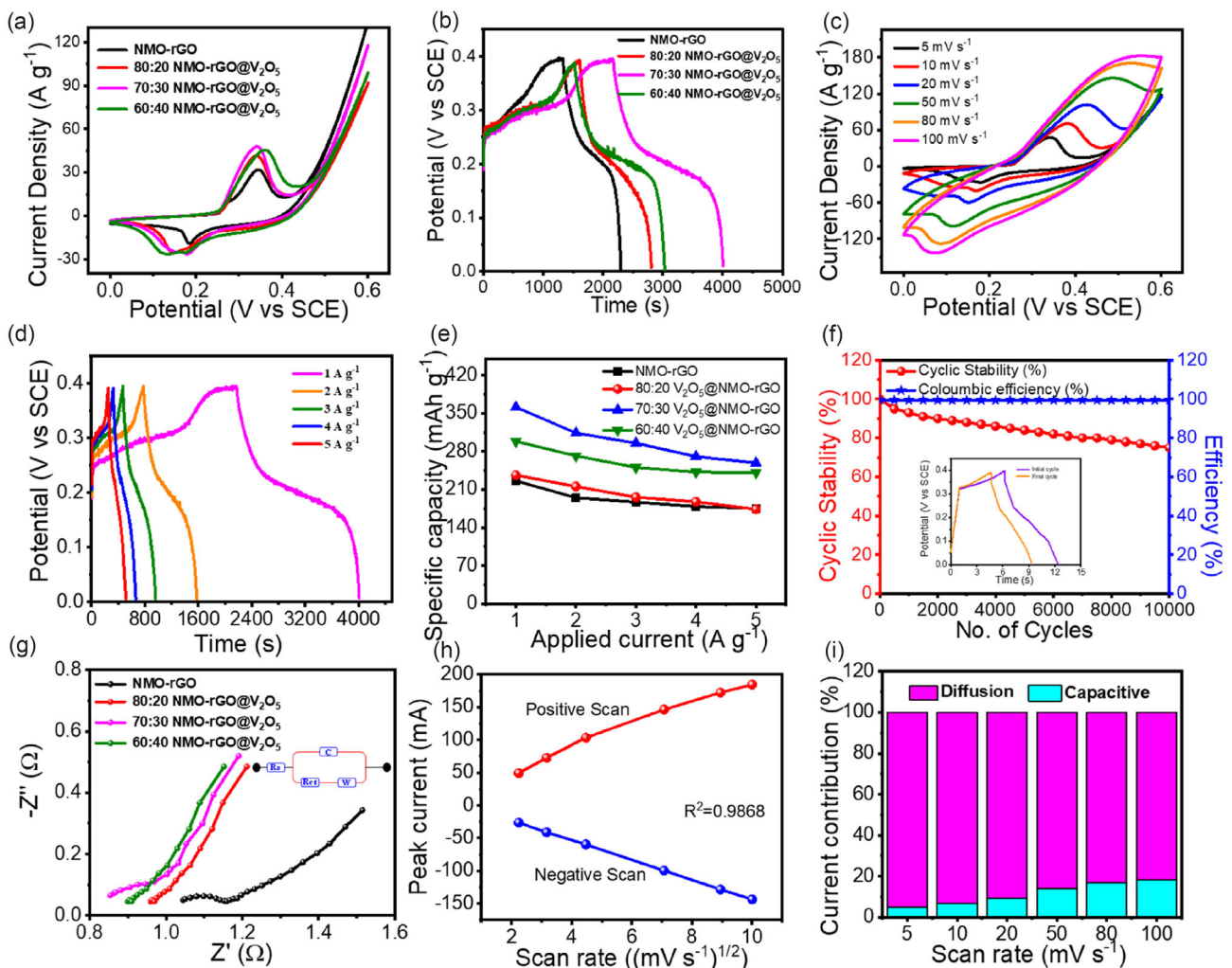


**Figure 4.** a,b) comparative CV and GCD profiles of NiMoO<sub>4</sub>-rGO, 80:20 NMO-rGO@V<sub>2</sub>O<sub>5</sub>, 70:30 NMO-rGO@V<sub>2</sub>O<sub>5</sub>, and 60:40 NMO-rGO@V<sub>2</sub>O<sub>5</sub> electrodes at scan rate of 5 mV s<sup>-1</sup> and current density of 1 A g<sup>-1</sup>, respectively. c,d) CV and GCD profiles with varying scan rate and current density of optimized 70:30 NMO-rGO@V<sub>2</sub>O<sub>5</sub> electrode, respectively. e) Variation of specific capacity with current density of NiMoO<sub>4</sub>-rGO, 80:20 NMO-rGO@V<sub>2</sub>O<sub>5</sub>, 70:30 NMO-rGO@V<sub>2</sub>O<sub>5</sub>, 60:40 NMO-rGO@V<sub>2</sub>O<sub>5</sub> electrodes. f) Cyclic stability retention and coulombic efficiency performance of optimized 70:30 NMO-rGO@V<sub>2</sub>O<sub>5</sub> electrode at current density of 30 A g<sup>-1</sup>. Inset shows initial and final cycles. g) Nyquist plots of NiMoO<sub>4</sub>-rGO, 80:20 NMO-rGO@V<sub>2</sub>O<sub>5</sub>, 70:30 NMO-rGO@V<sub>2</sub>O<sub>5</sub>, and 60:40 NMO-rGO@V<sub>2</sub>O<sub>5</sub> electrodes with equivalent circuit (Inset). h) Peak currents with respect to the square roots of the different scan rates of 70:30 NMO-rGO@V<sub>2</sub>O<sub>5</sub> electrodes. i) Total contribution of capacitive and diffusion-controlled charge storage of 70:30 NMO-rGO@V<sub>2</sub>O<sub>5</sub> electrode.

convincingly, revealing well-defined lattice fringes (0.36 and 0.308 nm) for the 70:30 electrode ultrafine particles, attributed to the (110) and (002) planes of V<sub>2</sub>O<sub>5</sub> and NiMoO<sub>4</sub>, respectively. This homogeneous nanoscale integration provides for efficient electron conduction pathways simultaneously with short ion diffusion lengths, both of which are paramount to achieving fast redox kinetics and ultimately high-rate performance. BET analysis shows that the optimized 70:30 composition has a greater specific surface area and mesoporous volume. These electrochemical findings are attributed to the synergistic effects of optimal nanostructure, high surface area and abundant accessible redox-active sites of the 70:30 electrode, which all lead to its superior specific capacity, rate capability and long-term cycling stability.

The specific capacity (Figure 4e) was calculated from the GCD study for NiMoO<sub>4</sub>-rGO, 80:20 NMO-rGO@V<sub>2</sub>O<sub>5</sub>, 70:30 NMO-rGO@V<sub>2</sub>O<sub>5</sub>, and 60:40 NMO-rGO@V<sub>2</sub>O<sub>5</sub> electrodes are 225.9,

236.3, 361.5, and 298.4 mAh g<sup>-1</sup> (from (Equation 1)) at minimum current density of 1 A g<sup>-1</sup>. It represents the variation of specific capacity with varying current density (1–5 A g<sup>-1</sup>), where the 70:30 NMO-rGO@V<sub>2</sub>O<sub>5</sub> electrode maintains a higher capacity compared to other compositions, emphasizing its superior rate performance at higher current density. The durability of the electrochemical performance of the optimized 70:30 NMO-rGO@V<sub>2</sub>O<sub>5</sub> electrode was evaluated through cyclic stability and coulombic efficiency tests at a greater current density of 30 A g<sup>-1</sup> over 10,000 charge–discharge cycles. As depicted in Figure 4f, the electrode maintains about 75% of its original specific capacity, revealing superior structural and electrochemical flexibility under extended cycling. This high coulombic retention reflects strong electrode–electrolyte interaction, redox kinetic stability, and low degradation of the active material. The uniform coulombic efficiency of ≈100% over the cycling time

ensures reversibility of the faradaic reactions and low side reactions in the system. The inset depicts charge discharge profiles of the initial and final cycle, emphasizing the nearly similar shape and symmetry, which further supports the stable capacitive character of the electrode.

XRD analysis (Figure S4a, Supporting Information) showed no notable changes in diffraction patterns after the stability test. However, SEM images (Figure S4b, c, Supporting Information) revealed partial collapse of nanorod-decorated microspheres, indicating deterioration of surface morphology and a compromised solid–liquid interface. After 10,000 charge–discharge cycles, stability declined significantly, as evidenced by reduced CV current (Figure S4d, Supporting Information), shorter discharge times (Figure S4e, Supporting Information), and increased solution and charge transfer resistances (Figure S4f, Supporting Information). These results confirm the 70:30 NMO-rGO@V<sub>2</sub>O<sub>5</sub> sample undergoes substantial morphological and electrochemical performance degradation during prolonged cycling. Table 1 shows that the comparative electrochemical study of NiMoO<sub>4</sub> based composite with the present study.

### 3.7. Electrochemical Impedance Spectroscopic Study

EIS was employed to evaluate the interfacial charge–transfer resistance and ion diffusion behavior of the NMO-rGO, 80:20 NMO-rGO@V<sub>2</sub>O<sub>5</sub>, 70:30 NMO-rGO@V<sub>2</sub>O<sub>5</sub>, and 60:40 NMO-rGO@V<sub>2</sub>O<sub>5</sub> electrodes in 2 M KOH electrolyte in the range between 100 kHz to 1 Hz as shown in the Nyquist plots in Figure 4g with an equivalent circuit (inset). Each Nyquist plot consists of a depressed semicircle in the high-to-medium frequency region and a linear Warburg tail in the low-frequency region, indicative of charge transfer and ion diffusion processes, respectively. The value of R<sub>s</sub> was evaluated for NMO-rGO, 80:20 NMO-rGO@V<sub>2</sub>O<sub>5</sub>, 70:30 NMO-rGO@V<sub>2</sub>O<sub>5</sub>, and 60:40 NMO-rGO@V<sub>2</sub>O<sub>5</sub> electrodes are 1.04, 0.96, 0.84, and 0.90 Ω cm<sup>-2</sup>, respectively. The value of R<sub>ct</sub> for NMO-rGO, 80:20 NMO-rGO@V<sub>2</sub>O<sub>5</sub>, 70:30 NMO-rGO@V<sub>2</sub>O<sub>5</sub>, and 60:40 NMO-rGO@V<sub>2</sub>O<sub>5</sub> electrodes are 0.15, 0.14, 0.12, and 0.13 Ω cm<sup>-2</sup>, respectively. Among all samples, the 70:30 NMO-rGO@V<sub>2</sub>O<sub>5</sub> electrode exhibits the lowest R<sub>s</sub> (0.84 Ω cm<sup>-2</sup>) and R<sub>ct</sub> (0.12 Ω cm<sup>-2</sup>) values, implying superior electrical conductivity and faster charge transfer kinetics at the electrode–electrolyte interface. The reduced semicircle diameter suggests minimal charge accumulation and enhanced electrochemical accessibility. The steep slope of the Warburg region further reflects improved ion diffusion within the porous electrode matrix, attributed to the synergistic effect of NMO-rGO conductive network and the high pseudocapacitive activity of V<sub>2</sub>O<sub>5</sub>. These observations confirm that the optimized 70:30 composition facilitates faster electron transport and electrolyte ion mobility, both of which are critical for achieving high rate capability and prolonged cycling stability in supercapacitor applications.<sup>[45]</sup> The comparative electrochemical performance of bare nickel foam with 70:30 NMO-rGO@V<sub>2</sub>O<sub>5</sub> electrode sample, including CV, GCD, and EIS study are displayed in Figure S5a–c, Supporting Information.

### 3.8. Kinetic Parameters Study of NMO-rGO@V<sub>2</sub>O<sub>5</sub> Composite

To explore the charge storage mechanism of the 70:30 NMO-rGO@V<sub>2</sub>O<sub>5</sub> electrode, a kinetic study was performed using CV data at varying scan rates (5–100 mV s<sup>-1</sup>). The linearity observed in the oxidation and reduction current peaks in Figure 4h, with a correlation coefficient (R<sup>2</sup>) value of ≈0.98, confirms that the majority of the current is generated from a diffusion-controlled electrochemical reaction. The relatively lower current increment with higher scan rates confirms kinetic limitations at faster potential sweeps, characteristic of diffusion-controlled redox reactions. This hybrid mechanism is beneficial for supercapacitor applications, offering a balance between high specific capacity and power capability. The relationship between positive scan peak current (i<sub>p</sub>) and their corresponding scan rates (v) from the CV study was evaluated using the power-law Equation (5)<sup>[46,47]</sup>

$$i_p = av^b \quad (5)$$

where the b-value offers insight into the charge storage process. A b-value of 0.5 signifies a diffusion-controlled process, while a value near 1.0 indicates capacitive (surface-controlled) behavior. In Figure S6a, Supporting Information, the plot of log(i) versus log(v) for the redox peaks yields a slope (b-value) of ≈0.53, signifying that the charge storage behavior is predominantly diffusion-controlled with some contribution from surface capacitive processes. This intermediate b-value reflects the pseudocapacitive nature of the material, attributed to redox reactions of V<sub>2</sub>O<sub>5</sub> and NiMoO<sub>4</sub>, where charge transfer and ion diffusion into the bulk dominate. The presence of rGO in the composite enhances electronic conductivity and partially promotes surface capacitive behavior. Nevertheless, the dominance of diffusion control indicates deep ion penetration into the porous electrode matrix during electrochemical cycling.<sup>[48]</sup>

To quantitatively distinguish the surface capacitive contribution from the diffusion-controlled process. The total current (i) at a constant potential (v) is the sum of the capacitive i<sub>cap</sub> and diffusion-controlled i<sub>diff</sub> contributions. This relationship can be represented by the following Equation (6) and (7)

$$i(v) = i_{cap} + i_{diff} \quad (6)$$

$$\text{where, } \begin{cases} i_{cap} = k_1 v \\ i_{diff} = k_2 v^{\frac{1}{2}} \end{cases} \quad (7)$$

To separate and quantify these contributions, the current response at different scan rates can be analyzed using the following Equation (8)

$$i(v) = k_1 v + k_2 v^{\frac{1}{2}} \quad (8)$$

where i(v) is the total current at potential, v is the scan rate, k<sub>1</sub>v represents the capacitive contribution, and k<sub>2</sub>v<sup>1/2</sup> represents the diffusion-controlled contribution.

Now, Equation (8) divided by  $v^{\frac{1}{2}}$  and the following Equation (9) stated as straight-line equation having  $k_1$  and  $k_2$  are the slope and y-intercept respectively, thus Equation (9) becomes

$$\frac{i(v)}{v^{\frac{1}{2}}} = k_1 v^{\frac{1}{2}} + k_2 \quad (9)$$

The bar graph (Figure 4i) presents a comparison of capacitive and diffusion contributions at different scan rates, revealing that capacitive effects become more dominant at higher scan rates, reaching nearly 25–30% at  $50\text{ mV s}^{-1}$ . However, diffusion processes still account for the major share of the overall current, confirming the material's pseudocapacitive characteristics. At lower scan rates ( $5\text{ mV s}^{-1}$ ), the diffusion contribution is as high as  $\approx 90\%$ , owing to sufficient time for electrolyte ions to penetrate deeper into the electrode material. As the scan rate increases, the time available for ion diffusion decreases, resulting in a relative enhancement of capacitive processes that occur on or near the surface. The synergistic combination of fast surface reactions and deep bulk redox processes ensures both high energy and power densities, validating the compositional and morphological optimization of the 70:30 electrode. The capacitive-diffusion separation map (Figure S6b, Supporting Information) visually confirms the spatial distribution of the capacitive and diffusion-controlled current densities across the CV window. The enhanced pseudocapacitive response in both peak and shoulder regions indicates redox activity primarily from  $\text{V}^{5+}/\text{V}^{4+}$  and  $\text{Ni}^{2+}/\text{Ni}^{3+}$  transitions. These findings clearly demonstrate that the 70:30 NMO-rGO@ $\text{V}_2\text{O}_5$  electrode exhibits an ideal balance between high-rate performance and electrochemical capacity, making it a promising candidate for advanced HSC applications.

#### 4. Fabrication and Performance Evaluation of Hybrid Supercapacitor Device

The HSC device was fabricated using an optimized sample 70:30 NMO-rGO@ $\text{V}_2\text{O}_5$  electrode exhibited as anode and AC as cathode in aqueous 2 M KOH electrolyte. The main objective of these concurrent experimental studies was to understand how both the HSC device and the AC electrode performed. First, we have tested AC electrode using CV and GCD study to evaluate its performance Figure S7a–c, Supporting Information. After that, we tested the rate capability of the NMO-rGO@ $\text{V}_2\text{O}_5$  //AC electrode through CV and GCD test in the potential of 0.8–1.6 V as demonstrated in Figure S8a–b, Supporting Information. CV curves of the positive electrode and negative electrode at  $5\text{ mV s}^{-1}$  show the potential windows and charge storage characteristics of each component (Figure 5a). The NMO-rGO@ $\text{V}_2\text{O}_5$  electrode has well-separated redox peaks, which is a clear sign of pseudocapacitive nature due to faradaic reactions involving  $\text{Ni}^{2+}/\text{Ni}^{3+}$  and  $\text{V}^{4+}/\text{V}^{5+}$  conversions. As a comparison, the AC electrode exhibited a CV shape that approached near-rectangular, verifying ideal double-layer capacitive behavior with fast charge adsorption–desorption. This marked electrochemical contrast in nature allows for the development of HSC that combines the high specific energy of pseudocapacitive materials with the stability and specific power attributes of EDLC-type electrodes. The quasirectangular shape with redox humps in the CV plots of the as-assembled NMO-rGO@ $\text{V}_2\text{O}_5$ //AC HSC device (Figure 5b) at scan rates ranging from 5 to  $100\text{ mV s}^{-1}$  indicates that double-layer capacitance and pseudocapacitance are involved in the charge storage. The CV shape at scan rates as high as  $100\text{ mV s}^{-1}$  confirms outstanding rate capability and rapid ion transport within the electrode. This

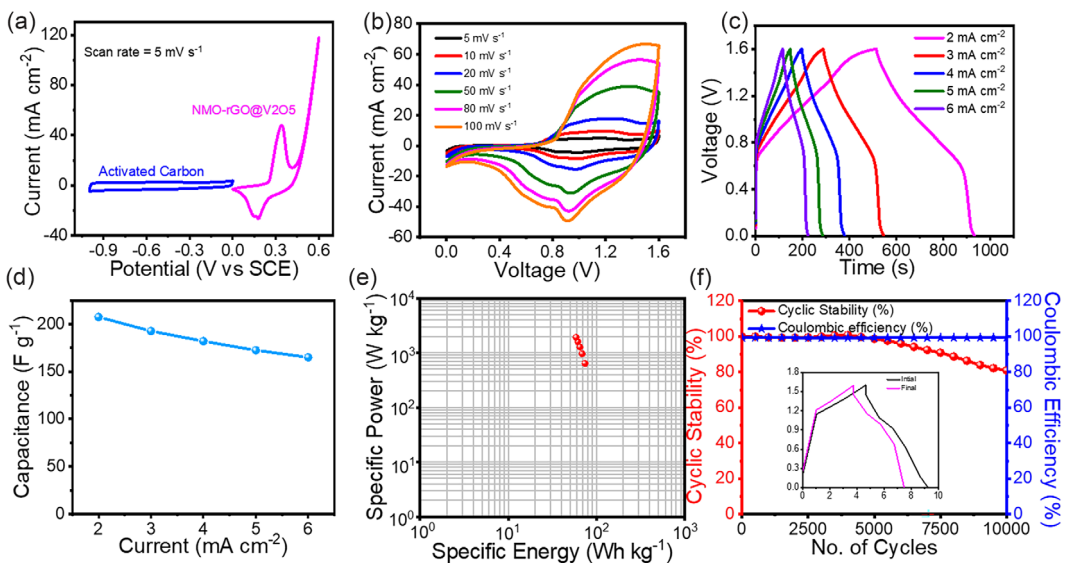


**Figure 5.** a) CV profiles of the individual positive NMO-rGO@ $\text{V}_2\text{O}_5$  and negative AC electrodes obtained at scan rate of  $5\text{ mV s}^{-1}$ . b) CV plots of the HSC device at varying different scan rates. c) GCD profiles of the HSC measured under different current densities ranging from 2 to  $6\text{ mA cm}^{-2}$ . d) Specific capacitance of the HSC as a function of different current density ( $2\text{--}6\text{ mA cm}^{-2}$ ). e) Ragone plot illustrating the relationship between specific energy and specific power of the HSC at multiple current densities ( $2\text{--}6\text{ mA cm}^{-2}$ ). f) Long-term cyclic stability and coulombic efficiency performance of the HSC device tested over 10,000 continuous GCD cycles at  $80\text{ mA cm}^{-2}$ . Inset shows the comparison between the first and last five cycles.

behavior is representative of the synergistic combination of conductive rGO, highly redox-active NiMoO<sub>4</sub> and V<sub>2</sub>O<sub>5</sub>, and mesoporous AC, allowing for rapid charge transport and site accessibility to electroactive species. Figure 5c reveals GCD curves of the HSC at different current densities (2–6 mA cm<sup>-2</sup>). The GCD curves illustrate almost symmetric triangular patterns with weak IR drops, verifying excellent capacitive characteristics and low internal device resistance. The general trend of decreasing discharge time with increasing current density is expected for HSCs and demonstrates the devices ability to sustain performance at elevated rate scenarios. Longer discharge time at a lower current density is attributed to an increase in specific capacitance owing to its improvement in ion diffusion and interaction with the electrode structural interior. Figure 5d shows the specific capacitance as a function of current density. The specific capacitance of the HSC device reached a high specific capacitance of 207.5 F g<sup>-1</sup> at 2 mA cm<sup>-2</sup>, which slowly down with the increase of current owing to kinetic restrictions and limitation in ion diffusion at high rates up to 165 F g<sup>-1</sup> at current density of 6 mA cm<sup>-2</sup>. This trend indicates the strong electrochemical kinetics and favorable conductivity, due to the designed nanostructure of the NMO-rGO@V<sub>2</sub>O<sub>5</sub> composite.

The Ragone plot (Figure 5e) shows the tradeoff between specific energy and specific power for the HSC. Particularly, the HSC device provides specific energy up to 73.77 Wh kg<sup>-1</sup> and specific power 640 W kg<sup>-1</sup> at a current density of 2 mA cm<sup>-2</sup>, while maintaining a significant specific energy of 58.66 Wh kg<sup>-1</sup> and even high specific power 1920 W kg<sup>-1</sup> at a current density of 6 mA cm<sup>-2</sup> from Equation (2) and (3). This is indicative of the HSC designs ability to combine the high capacity redox characteristics of NiMoO<sub>4</sub> and V<sub>2</sub>O<sub>5</sub> with the quick charge transfer functions of rGO and AC. To further confirm the long-term cycling durability, the HSC device was tested for 10,000 continuous charge-discharge cycles at 80 mA cm<sup>-2</sup> (Figure 5f). Impressively, the device kept at least 81% of its original capacitance, along with close to 100% of coulombic efficiency during the full 10,000 cycle assessment, demonstrating remarkable electrochemical stability and reversibility. The corresponding inset GCD profiles comparing the first and last cycles reveal almost small amount of

distortion, indicating that the electrode architecture has maintained structural integrity and active materials are not being compromised. Figure S9, Supporting Information shows the structural, morphological and electrochemical analysis of positive electrode (70:30 NMO-rGO@V<sub>2</sub>O<sub>5</sub>) of the HSC device after 10,000 cycles. The XRD pattern (Figure S9a, Supporting Information) shows that no substantial changes in the electrode sample even after 10,000 cycles. Figure S9b, c, Supporting Information shows SEM images of the positive electrode (70:30 NMO-rGO@V<sub>2</sub>O<sub>5</sub>) of the HSC device. SEM images show that, although the electrode largely retains its spherical architecture but the nanorods have collapsed, which adversely affects the cyclic stability of the 70:30 NMO-rGO@V<sub>2</sub>O<sub>5</sub> electrode sample, resulting in decreased performance. The comparative CV, GCD characteristics of the 70:30 NMO-rGO@V<sub>2</sub>O<sub>5</sub> //AC HSC device before and after cyclic stability testing is depicted in Figure S9d, e, Supporting Information. The EIS analysis HSC device, presented in the Figure S9f, Supporting Information, compares the impedance behavior before and after long-term cycling stability testing. The *R<sub>s</sub>* value of symmetric device are 0.85 and 0.98 before and after cyclic stability over 10,000 cycles. Before cycling, the device exhibits a small semicircle, corresponding to a low *R<sub>ct</sub>* is 1.12 Ω cm<sup>-2</sup>, signifying excellent electrical conductivity and good electrode–electrolyte interaction. The nearly vertical line in the low-frequency region reflects ideal capacitive behavior with efficient ion diffusion pathways through the porous electrode structure. After 10,000 continuous GCD cycles, there is only a slight increase in the semicircle diameter, indicating a minor rise in *R<sub>ct</sub>* (1.2 Ω cm<sup>-2</sup>). The inset of Figure S9f, Supporting Information shows the equivalent circuit matching with the EIS data of the HSC device before and after cyclic stability over 10,000 cycles. It comprises *R<sub>s</sub>*, which accounts for the electrolyte ionic conductivity as well as experimental setup resistances. Also, the electrode–electrolyte interface processes are modeled using a parallel combination of *R<sub>ct</sub>*, *C*, and *W*. The stable Warburg impedance suggests that the device maintains good ion diffusion properties even after extensive cycling, highlighting its suitability for long term electrochemical applications. This suggests that the electrode–electrolyte interface remains largely intact, and the composite maintains favorable

**Table 2.** Comparative study of supercapacitor devices and their primary characteristics.

Positive electrode	Negative Electrode	Specific capacitance [F g <sup>-1</sup> ]	Specific Energy [Wh kg <sup>-1</sup> ]	Specific Power [W kg <sup>-1</sup> ]	Potential Window [V]	Cyclic stability	Electrolyte	Reference
NiMoO <sub>4</sub>	AC	158.3	56.3	421	0.0 to 1.6	104% after 10,000 cycles	2M KOH	[18]
NiMoO <sub>4</sub> @C	AC	201.3	72.4	851.8	0.0 to 1.6	98% after 4000 cycles	2M KOH	[51]
NiMoO <sub>4</sub>	AC	151.7	60.9	850	0.0 to 1.7	85.7% after 10,000 cycles	2M KOH	[52]
CoMoO <sub>4</sub>	AC	112.6	40	685.8	0.0 to 1.6	86.9% after 5000 cycles	2M KOH	[53]
NiMoO <sub>4</sub> /rGO	AC	192.3	48.2	887	0.0 to 1.8	75% after 10,000 cycles	2M KOH	[54]
CoMoO <sub>4</sub> /rGO	AC	264	82.7	3700	0.0 to 1.6	85% after 5000 cycles	6M KOH	[55]
NiMoO <sub>4</sub> /rGO	AC	138	60.2	750.5	0.0 to 1.6	98.5% after 10,000 cycles	1M KOH	[56]
NMO-rGO@V <sub>2</sub> O <sub>5</sub>	NMO-rGO@V <sub>2</sub> O <sub>5</sub>	70.5	28.33	2040	0.0 to 1.7	114% after 15,000 cycles	2M KOH	This work
NMO-rGO@V <sub>2</sub> O <sub>5</sub>	AC	207.5	73.77	640	0.0 to 1.7	81% after 10,000 cycles	2M KOH	

electrochemical kinetics. This excellent performance benefits from the excellent interfacial contact, structural integrity, and redox reversibility of NMO-rGO@V<sub>2</sub>O<sub>5</sub> hybrid. This integration offers a number of advantages, including high specific capacitance, high rate capability, high specific energy and specific power, and long-term stability. **Table 2.** shows the comparative study of supercapacitor devices and their primary characteristics. Additionally, a symmetric device configuration comprising 70:30 NMO-rGO@V<sub>2</sub>O<sub>5</sub> //70:30 NMO-rGO@V<sub>2</sub>O<sub>5</sub> electrodes was tested in 2 M KOH electrolyte. Detailed electrochemical characteristics of this symmetric configuration are provided in the supporting information Figure S10 and S11, Supporting Information.

## 5. Conclusion

This notable progress in the preparation of the novel ternary NMO-rGO@V<sub>2</sub>O<sub>5</sub> composite paves a way for constructing excellent electrode materials for HSC. Through the deliberate incorporation of the redox-active NiMoO<sub>4</sub>, the highly conductive and surface-enriched rGO, and the pseudocapacitive V<sub>2</sub>O<sub>5</sub>, the resultant composite demonstrates highly extensive synergistic effects that overcome the drawbacks of each individual constituent. The as-synthesized optimized NMO-rGO@V<sub>2</sub>O<sub>5</sub> composite shows a specific capacity of 361.5 mAh g<sup>-1</sup> at the lower current density of 1 A g<sup>-1</sup>, excellent rate performance and long-term cyclical stability with a retention of 75% after 10,000 cycles. When used in HSC (NMO-rGO@V<sub>2</sub>O<sub>5</sub>//AC) device configuration, it obtains ultra-high specific energy of 73.77 Wh kg<sup>-1</sup> and ultra-high specific power of 1920 W kg<sup>-1</sup>, surpassing the majority of traditional electrode configurations. Collectively, these findings provide fundamental insights into the promise of NMO-rGO@V<sub>2</sub>O<sub>5</sub> as a novel candidate, next-generation electrode material toward advanced energy storage technologies, and pave the way toward its eventual practical implementation in high-performance supercapacitors.

## Acknowledgements

D.S.S. is thankful to the Chhatrapati Shahu Maharaj Research, Training and Human Development Institute (SARTHI), Government of Maharashtra, India for providing financial support (SARTHI/fellowship/CSMNRF-2023/2024-25/1773). G.M.L. is thankful to Central Analytical Research Facility (CARF), QUT, Australia for providing characterization facilities.

## Conflict of Interest

The authors declare no conflict of interest.

## Data Availability Statement

The data that support the findings of this study are available from the corresponding author upon reasonable request.

**Keywords:** excellent specific energy and power • high specific capacity • hybrid supercapacitor devices • ternary NiMoO<sub>4</sub>-rGO@V<sub>2</sub>O<sub>5</sub> nanocomposite

- [1] H. Brugger, W. Eichhammer, N. Mikova, E. Döñitz, *Energy Policy* **2021**, *152*, 112216.
- [2] C. D. Chavare, D. S. Sawant, S. V. Gaikwad, A. V. Fulari, H. R. Kulkarni, D. P. Dubal, G. M. Lohar, *J. Mater. Chem. A* **2025**, *13*, 6993.
- [3] A. Rode, T. Carleton, M. Delgado, M. Greenstone, T. Houser, S. Hsiang, A. Hultgren, A. Jina, R. E. Kopp, K. E. McCusker, I. Nath, J. Rising, J. Yuan, *Nature* **2021**, *598*, 308.
- [4] J. Liu, *J. Supercomput.* **2022**, *78*, 1624.
- [5] A. Payman, S. Pierfederici, F. Meibody-Tabar, *Energy Convers. Manage.* **2008**, *49*, 1637.
- [6] D. S. Sawant, O. C. Pore, S. B. Kulkarni, G. M. Lohar, in *3D Printing: Fundamentals to Emerging Applications*, **2023**, pp. 213–230, <https://doi.org/10.201/9781003296676-14/3D-PRINTED-CARBON-BASED-NANOMATERIALS-SUPERCAPACITORS-DIGAMBAR-SAWANT-ONKAR-PORE-SHRINIVAS-KULKARNI-GAURAV-LOHAR>.
- [7] J. Liu, J. Wang, C. Xu, H. Jiang, C. Li, L. Zhang, J. Lin, Z. X. Shen, *Adv. Sci.* **2018**, *5*, 1700322.
- [8] O. C. Pore, A. V. Fulari, R. V. Shejwal, V. J. Fulari, G. M. Lohar, *Chem. Eng. J.* **2021**, *426*, 131544.
- [9] P. Sinha, K. K. Kar, in *Handbook of Nanocomposite Supercapacitor Materials II* (Eds: K. Kar), Springer Series in Materials Science, Vol. 302. Springer, Cham **2020**, [https://doi.org/10.1007/978-3-030-52359-6\\_1](https://doi.org/10.1007/978-3-030-52359-6_1).
- [10] F. Bibi, G. Ong, A. J. Khan, M. Khalid, A. Numan, in *Advanced Electrode Materials for Supercapacitors* (Eds: R. Bhatia, N. Singh), Elsevier, Amsterdam **2024**, <https://doi.org/10.1016/b978-0-443-15478-2.00005-x>.
- [11] N. Kumar, S. B. Kim, S. Y. Lee, S. J. Park, *Nanomaterials* **2022**, *12*, 3708.
- [12] A. P. De Moura, L. H. De Oliveira, I. L. V. Rosa, C. S. Xavier, P. N. Lisboa-Filho, M. S. Li, F. A. La Porta, E. Longo, J. A. Varella, *Sci. World J.* **2015**, *2015*, 315084.
- [13] Y. Su, C. Wu, Y. Song, Y. Li, Y. Guo, S. Xu, *Appl. Surf. Sci.* **2019**, *488*, 134.
- [14] J. H. Li, Y. C. Chen, Y. S. Wang, W. H. Ho, Y. J. Gu, C. H. Chuang, Y. Da Song, C. W. Kung, *ACS Appl. Energy Mater.* **2020**, *3*, 6258.
- [15] B. Yin, L. Hao, T. Wei, C. Wang, B. Zhu, X. Li, Q. Yang, *Chem. Eng. J.* **2022**, *450*, 138224.
- [16] D. Zhou, P. Cheng, J. Luo, W. Xu, J. Li, D. Yuan, *J. Mater. Sci.* **2017**, *52*, 13909.
- [17] O. C. Pore, A. V. Fulari, C. D. Chavare, D. S. Sawant, S. S. Patil, R. V. Shejwal, V. J. Fulari, G. M. Lohar, *Chem. Phys. Lett.* **2023**, *824*, 140551.
- [18] D. S. Sawant, S. V. Gaikwad, A. V. Fulari, M. Govindasamy, S. B. Kulkarni, D. P. Dubal, G. M. Lohar, *Small* **2025**, *21*, 2500080.
- [19] J. Yu, H. Su, C. Shi, G. Qiu, L. Bai, Z. Li, *Electrochim. Acta* **2023**, *471*, 143392.
- [20] Z. Li, C. Shi, J. Yu, L. Bai, *Appl. Surf. Sci.* **2024**, *669*, 160534.
- [21] E. Murugan, S. Govindaraju, S. Santhoshkumar, *Electrochim. Acta* **2021**, *392*, 138973.
- [22] J. Li, Y. Zou, L. Jin, F. Xu, L. Sun, C. Xiang, *J. Energy Storage* **2022**, *50*, 104639.
- [23] X. Liu, K. Zhang, B. Yang, W. Song, Q. Liu, F. Jia, S. Qin, W. Chen, Z. Zhang, J. Li, *Mater. Lett.* **2016**, *164*, 401.
- [24] Y. Li, J. Jian, L. Xiao, H. Wang, L. Yu, G. Cheng, J. Zhou, M. Sun, *Mater. Lett.* **2016**, *184*, 21.
- [25] D. B. Mane, O. C. Pore, D. S. Sawant, D. V. Rupnavar, R. V. Shejwal, S. H. Mujawar, L. D. Kadam, R. V. Dhekale, G. M. Lohar, *Appl. Phys. A* **2023**, *129*, 1.
- [26] V. U. Shankar, D. Govindarajan, R. Gopalakrishnan, T. Maiyalagan, M. J. Salethraj, *Mater. Today Commun.* **2021**, *27*, 102357.
- [27] D. Navas, S. Fuentes, A. Castro-Alvarez, E. Chavez-Angel, *Gels* **2021**, *7*, 275.
- [28] M. B. Arbia, H. Helal, E. Comini, *Nanomaterials* **2024**, *14*, 359.
- [29] Y. Zhu, G. Kong, Y. Pan, L. Liu, B. Yang, S. Zhang, D. Lai, C. Che, *Chin. Chem. Lett.* **2022**, *33*, 4541.
- [30] Q. Hu, W. Li, B. Xiang, X. Zou, J. Hao, M. Deng, Q. Wu, Y. Wang, *Electrochim. Acta* **2020**, *337*, 135826.
- [31] H. Su, C. Niu, R. Zhang, M. Huang, Z. Li, *J. Alloys Compd.* **2025**, *1010*, 178074.
- [32] M. Huang, J. Yu, H. Su, Z. Wu, Z. Li, *Appl. Surf. Sci.* **2025**, *681*, 161547.
- [33] A. Shameem, P. Devendran, A. Murugan, V. Siva, S. A. Bahadur, *J. Phys. Chem. Solids* **2023**, *179*, 111392.
- [34] M. Nasrollahzadeh, F. Babaei, P. Fakhri, B. Jaleh, *RSC Adv.* **2015**, *5*, 10782.

- [35] D. Govindarajan, V. U. Shankar, R. Gopalakrishnan, *J. Mater. Sci.: Mater. Electron.* **2019**, *30*, 16142.
- [36] D. Ghosh, S. Giri, C. K. Das, *Nanoscale* **2013**, *5*, 10428.
- [37] Y. Li, J. Jian, Y. Fan, H. Wang, L. Yu, G. Cheng, J. Zhou, M. Sun, *RSC Adv.* **2016**, *6*, 69627.
- [38] C. Zhang, X. Geng, S. Tang, M. Deng, Y. Du, *J. Mater. Chem. A* **2017**, *5*, 5912.
- [39] B. Hu, L. Li, X. Xiong, L. Liu, C. Huang, D. Yu, C. Chen, *J. Solid State Electrochem.* **2019**, *23*, 1315.
- [40] B. A. Khan, R. Hussain, A. Shah, A. Mahmood, M. Z. U. Shah, J. Ismail, S. ur Rahman, M. Sajjad, M. A. Assiri, M. Imran, M. S. Javed, *Ceram. Int.* **2022**, *48*, 5509.
- [41] Z. A. Alothman, *Materials* **2012**, *5*, 2874.
- [42] Z. Li, J. Yu, C. Shi, H. Su, L. Bai, *J. Energy Storage* **2024**, *91*, 112082.
- [43] D. Guo, Y. Luo, X. Yu, Q. Li, T. Wang, *Nano Energy* **2014**, *8*, 174.
- [44] S. Anantharaj, S. Noda, *J. Mater. Chem. A* **2022**, *10*, 9348.
- [45] A. C. Lazanas, M. I. Prodromidis, *ACS Meas. Sci. Au* **2023**, *3*, 162.
- [46] K. O. Oyedotun, A. A. Mirghni, O. Fasakin, D. J. Tarimo, V. N. Kitenge, N. Manyala, *Energy Fuels* **2021**, *35*, 20309.
- [47] D. K. Denis, X. Sun, J. Zhang, Y. Wang, L. Hou, J. Li, C. Yuan, *ACS Appl. Energy Mater.* **2020**, *3*, 3955.
- [48] M. Z. Iqbal, S. Zakar, M. Tayyab, S. S. Haider, M. Alzaid, A. M. Afzal, S. Aftab, *Appl. Nanosci.* **2020**, *10*, 3999.
- [49] Z. Yin, S. Zhang, Y. Chen, P. Gao, C. Zhu, P. Yang, L. Qi, *J. Mater. Chem. A* **2015**, *3*, 739.
- [50] H. M. Fahad, F. Shaheen, R. Ahmad, M. H. Aziz, A. A. Ifseisi, Q. Huang, *Electrochim. Acta* **2024**, *477*, 143756.
- [51] Z. Wang, G. Wei, K. Du, X. Zhao, M. Liu, S. Wang, Y. Zhou, C. An, J. Zhang, *ACS Sustainable Chem. Eng.* **2017**, *5*, 5964.
- [52] S. Peng, L. Li, H. B. Wu, S. Madhavi, X. W. Lou, *Adv. Energy Mater.* **2015**, *5*, 1401172.
- [53] D. Yu, Z. Zhang, Y. Teng, Y. Meng, X. Zhao, X. Liu, *J. Alloys Compd.* **2020**, *835*, 155244.
- [54] M. Beemarao, P. Kanagambal, K. Ravichandran, P. Rajeswaran, I. M. Ashraf, U. Chalapathi, S. H. Park, *Inorg. Chem. Commun.* **2023**, *153*, 110853.
- [55] D. Guo, Z. Guan, D. Hu, L. Bian, Y. Song, X. Sun, X. Liu, *J. Mater. Sci.* **2021**, *56*, 10965.
- [56] T. Nandagopal, G. Balaji, S. Vadivel, *J. Electroanal. Chem.* **2023**, *928*, 116944.

---

 Manuscript received: May 31, 2025

Revised manuscript received: August 15, 2025

Version of record online: